Journal of Nuclear Materials 378 (2008) 220–228

Contents lists available at ScienceDirect

Journal of Nuclear Materials

journal homepage: www.elsevier.com/locate/jnucmat

Oxidation of aluminum alloy cladding for research and test reactor fuel ☆

Yeon Soo Kim [a,*], G.L. Hofman [a], A.B. Robinson [b], J.L. Snelgrove [a], N. Hanan [a]

[a] Argonne National Laboratory, Nuclear Engineering, 9700 South Cass Avenue, Argonne, IL 60439, USA
[b] Idaho National Laboratory, P.O. Box 1625, Idaho Falls, ID 83415-6188, USA

ARTICLE INFO

Article history:
Received 29 January 2008
Accepted 13 June 2008

ABSTRACT

The oxide thicknesses on aluminum alloy cladding were measured for the test plates from irradiation tests RERTR-6 and 7A in the ATR (advanced test reactor). The measured thicknesses were substantially lower than those of test plates with similar power from other reactors available in the literature. The main reason is believed to be due to the lower pH (pH 5.1–5.3) of the primary coolant water in the ATR than in the other reactors (pH 5.9–6.5) for which we have data. An empirical model for oxide film thickness predictions on aluminum alloy used as fuel cladding in the test reactors was developed as a function of irradiation time, temperature, surface heat flux, pH, and coolant flow rate. The applicable ranges of pH and coolant flow rates cover most research and test reactors. The predictions by the new model are in good agreement with the in-pile test data available in the literature as well as with the RERTR test data measured in the ATR.

1. Introduction

Since the main purpose of research and test reactors is to produce neutrons rather than power, they require fuels that can operate at high-power density (and, therefore, high cladding surface heat flux) with low parasitic neutron absorption. Consequently, aluminum alloys are used as fuel cladding material for most of these reactors, due to its high thermal conductivity and low neutron absorption cross section. Of course, the fuel must operate at low-enough temperatures to be compatible with aluminum. Formation of oxides on the cladding affects fuel performance by increasing fuel temperature. The thermal conductivity of the oxide is ~10-fold lower than that of aluminum. An oxide film of 1-μm thickness increases fuel temperature by approximately 1 °C for a surface heat flux of 2.25 MW/m^2. If the oxide thickens excessively, it poses a considerable performance issue.

There are oxide thickness prediction models based on out-of-pile data [1–5]. All of them are power law models and were developed for data from out-of-pile loop tests. Irradiation effects were not considered in these models. These models are inconsistent among themselves. In addition, their application ranges are limited. They are applicable to limited situations with the coolant pH, coolant flow rate, and fuel life. A major adjustment is necessary to apply any of these models to various in-pile situations.

An empirical model [6] consisting of correlations predicting the oxide film thickness on aluminum alloy cladding for both out-of-pile and in-pile tests was developed several years ago as a function of test time, oxide-water interface temperature, heat flux at cladding surface, coolant water pH, and coolant flow rate for the relevant coolant channel using the measured data from out-of-pile [1–5,7] and from in-pile tests available in the literature [8–12]. After this empirical model was developed, oxide thickness measurements became available from the RERTR (reduced enrichment for research and test reactors) tests in the advanced test reactor (ATR). The model has been updated using these measured data. However, the model with another set of parameters available in Ref. [6] is still applicable to out-of-pile tests. The model predictions are consistent with the RERTR test data as well as the in-pile data in the literature.

2. Experimental data

The oxide thickness data were obtained from two irradiation tests, i.e., RERTR-6 and 7A, in the ATR. The test samples were plates containing a fuel meat of 81.3 × 18.5 × 0.64 mm encapsulated in aluminum alloy Al 6061 cladding to make the final size of 101.6 (length) × 25.4 (width) × 1.4 (thickness) mm. The nominal alloy composition of Al 6061 is Cu (0.15–0.4) + Si (0.4–0.8) + Fe (0.7) + Mn (0.15) + Mg (0.8–1.2) + Zn (0.25) + Cr (0.04–0.35) + Ti (0.15) + Al (remainder), where the numbers in parentheses are in wt%. All test plates were autoclaved in water at 185 °C and 1-MPa for 4 h to produce an oxide layer of about 1-μm thickness prior to loading them into the test capsules; the oxidation is commonly called 'prefilming'.

☆ Work supported by US Department of Energy, Office of Global Threat Reduction, National Nuclear Security Administration (NNSA), under contract No. DE-AC-02-06CH11357.

* Corresponding author. Tel.: +1 630 252 3173; fax: +1 630 252 5161.
E-mail address: yskim@anl.gov (Y.S. Kim).

0022-3115/$ - see front matter © 2008 Elsevier B.V. All rights reserved.
doi:10.1016/j.jnucmat.2008.06.032

Table 1
Test parameters of RERTR-6 and 7A plates

Operation parameter	RERTR-6	RERTR-7A
Irradiation time (t in d)	135	90
pH	5.1–5.3	5.1–5.3
Coolant speed (v_c in m/s)	2.8	10.8
Heat flux (q in MW/m^2)[a]	B2 (1 → 0.75)	B2 (2.1 → 2.0)
	B5 (1.1 → 0.77)	
	B7 (0.82 → 0.73)	B7 (2.3 → 2.1)
Oxide–water interface temperature	B2 (114 → 98)	B2 (99 → 90)
($T_{x/w}$ in °C)[a]	B5 (120 → 100)	
	B7 (107 → 93)	B7 (106 → 101)

[a] Heat flux and oxide–water interface temperature were decreased linearly from the beginning to the end of the test.

The experiment basket comprised four capsules, A, B, C, and D, each containing eight plates in two rows. The plates were loaded in the capsules by standing in the length direction axially and sideways to the reactor core so that one side of the plate width had a higher power than the other side. The ATR has a downward coolant flow so the coolant enters at A capsule and exits at D capsule. The coolant flow rate in the test capsule was designed to have a flow velocity of 2.8 m/s for all plates in the RERTR-6 test and 10.8 m/s in RERTR-7A test. Table 1 compares the test parameters between RERTR-6 and 7A tests. Because of the difference in flow rate, although the surface heat fluxes are larger for RERTR-7A than RERTR-6, oxide–water interface temperatures are similar for both tests. The pH of the water coolant was maintained in a range 5.1–5.3 for both tests. This pH level is exceptionally lower than those of other reactors whose results we used in this paper. The irradiation test durations were 135 days over three cycles for the RERTR-6 test and 90 days over two cycles for the RERTR-7A test.

Some of the irradiated plates were cut and metallographically examined. An example of oxide film morphology is shown in Fig. 1. The scanning electron micrograph in the inset [12] shows that numerous thin cracks were visible in the cross section of the oxide. Similar cracked oxide morphology was also observed frequently in other reactor tests [8–11,13]. The cracks seem to be uniformly distributed on the oxide surface [13]. The cracks in the oxide films are believed to form during irradiation by hydration of the oxides. More importantly, the oxide in Fig. 1 appears to be composed of different phases with different brightness.

After irradiation, using the eddy current method [14], oxide thickness was measured at 9 locations on both sides of the plates, as shown in Fig. 2. The oxide thickness measurements for all test plates of RERTR-6 are given in Table 2 and those of RERTR-7A are given in Table 3. We have noticed that the thickness data tend to be more scattered and irregular measurements occur more frequently for uneven plate surfaces than the smooth ones and for thinner oxides than 10 μm. The monolithic fuel plates have more uneven plate surfaces than the dispersion fuel plates. The measurement errors were in the range ±10% for the dispersion fuel plates and ±25% for the monolithic fuel plates.

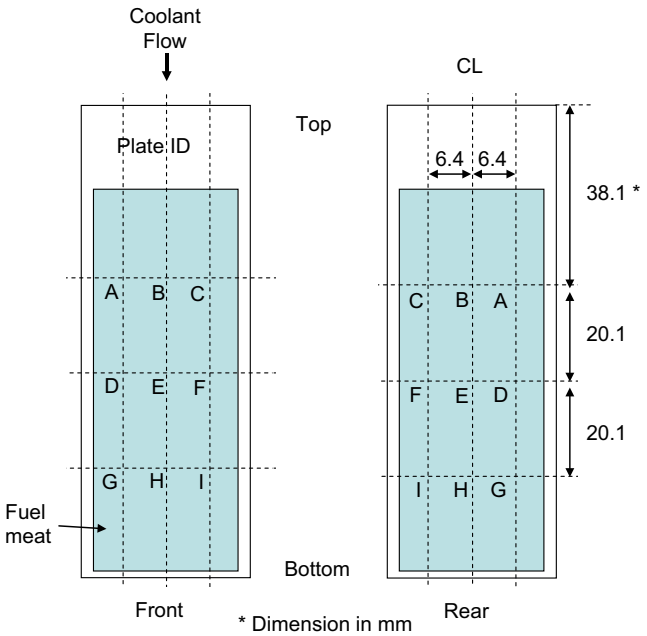

Fig. 2. Schematic illustration of oxide measurement locations on a plate for RERTR-6 and 7A tests.

It is obvious that some plates have irregular oxide thickness on the same face of the plate (see Tables 2 and 3). The reason cannot be readily explained. The measured oxide thicknesses thinner than the prefilm oxide thickness may be due to measurement errors or the oxide dissolution being greater than its growth rate. At this time, however, only more-accurate measurements can reveal the real reason. Therefore, the less-than-1-μm oxide thicknesses are considered tentative.

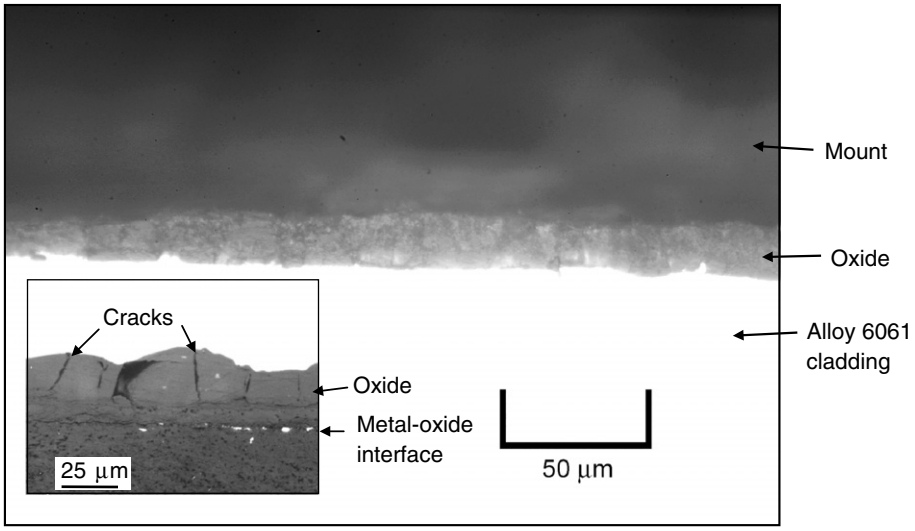

Fig. 1. Oxide morphology on cross section of C7 plate from RERTR-7A test. The micrograph in the inset is from the SIMONE LC-04 test showing cracks in the oxide [12].

Table 2
RERTR-6 oxide thickness measurements at 18 locations shown in Fig. 1

Plate ID	Fuel type	Oxide thickness (μm)									
		Front Rear	A A	B B	C C	D D	E E	F F	G G	H H	I I
A2	D[a]	Front	2	2.2	1.5	2	2.7	1.9	1.7	2.6	2
		Rear	0.4	2.7	3.2	0.8	2.8	1.6	3	2.4	4.4
A4	M[b]	Front	1.3	1.7	2.2	1.2	0.4	5.3	0.8	0.4	6.9
		Rear	1.6	3	5	2.1	3.2	2.4	3.8	3.3	2.9
A5	D	Front	2	2.5	2.6	1.7	3.4	2.1	2.3	3.2	2
		Rear	1.2	1.9	1	1.8	1.3	2.3	1.3	2.2	0.7
A6	M	Front	5.6	6.4	4.7	4.1	6.1	4.4	5.6	7.1	4.1
		Rear	5.4	2.8	3.6	5.2	2.3	3.4	4.7	3.2	1.6
A8	M	Front	4.8	3.5	10.3	5.5	4.6	6.6	6.9	4.8	8.8
		Rear	4.1	4.6	5.9	7.2	3.8	10	7	7.7	7.7
B1	D	Front	3.6	3	2.2	3.8	3.2	1.9	5.2	4.4	2.2
		Rear	3.6	5.3	4.2	3.8	3.7	3.8	4.6	4.4	3.4
B2	D	Front	2.8	3	2.6	2.4	4.3	4.6	1.5	4.3	4
		Rear	1.5	5.3	1.5	1.6	3.3	1.7	1	2.1	2.3
B3	D	Front	6.7	4.2	4.2	4.5	4.6	0.4	0.4	0.7	3.9
		Rear	4.6	3.8	3	4.2	5	2.2	4	3.9	4.3
B4	M	Front	7	5.6	5.6	13.2	6	4.2	7.7	4.8	6.9
		Rear	5.3	2.1	4.8	9	4.8	5.4	10.6	5.8	4.5
B5	D	Front	3.5	5.1	3.3	2.7	3.5	1	2.4	2.7	1.2
		Rear	6	4.8	4.6	4.4	5.6	5.1	4.6	4.6	2.3
B6	M	Front	3.5	2.8	3.1	4.9	4.8	2.8	7.3	5.1	3.5
		Rear	4.4	4.1	5.2	4.9	4.8	5.4	5.1	5	3
B7	M	Front	4.9	2	1.9	6.5	3.7	4.6	2.3	3.2	3.3
		Rear	3.7	3	3.3	4	4.6	1.5	4.4	6.1	3.3
B8	D	Front	3.2	3.9	2.7	1.7	1.8	1	1.5	2.7	2.5
		Rear	1.3	2.2	1.7	3.8	2.8	2.4	1.5	3.2	2.9
C1	D	Front	1.7	5.8	3.7	4	5.4	3.2	3.4	4.7	3.8
		Rear	2.5	3	3.8	1.8	1.9	3	4.8	4.1	3.2
C2	D	Front	1.5	3.6	1.6	3.5	3.2	1.7	3.1	2.5	2.5
		Rear	3.2	2.9	2.3	1.6	3.5	3.2	1.8	4.7	3.1
C3	D	Front	5.3	2.9	3.4	2.1	5.1	4.4	4.7	4	2.7
		Rear	3.8	3.7	4.2	4.3	5.1	4.7	3.2	4.1	2.9
C4	M	Front	5.7	3.4	5.2	5.4	3.7	4	3	3.6	3.1
		Rear	12.1	4.8	5.4	7.1	5.1	3.3	7.9	6.9	4.3
C5	D	Front	3.2	5.2	3.8	4.1	5.5	7	3.1	5.7	5.4
		Rear	3.7	3.9	3.2	13.4	5.1	2.9	9.7	3.9	5
C6	M	Front	2.2	3.5	4.4	4.1	3	5.8	3.4	2.7	4.1
		Rear	5.1	3.2	5.7	10.7	4	3.8	6.3	4	4
C7	D	Front	3.5	4.3	6	4.1	4	5.9	4.4	4.8	6.1
		Rear	6.7	5.7	3.3	5.8	4.8	3.6	6.2	4.5	4.5
D1	M	Front	2.9	2.3	2.1	3.1	4.7	2.8	2.3	4.7	3.9
		Rear	4.1	3	4.1	5.7	3	3.6	3.6	3	2.7
D2	D	Front	3.6	5.1	3.7	5.4	4	3.6	6.5	6.3	3.2
		Rear	5.1	4.2	2.1	3.9	3.9	2.7	3.5	4.4	4.1
D3	D	Front	4.8	4.4	6.1	3.3	5.1	4.1	4.5	4.7	2.6
		Rear	3.1	4	3.2	4.5	4.9	4.5	3.3	3	4.4
D5	D	Front	5.4	5.3	3	4.4	6.6	3.3	5.7	4.1	6.8
		Rear	1.7	3.8	1.4	3.5	3.2	2.6	4.2	2.8	1.5
D7	M	Front	5.3	2.5	4.1	4.3	1.1	4	5.1	1.4	3.6
		Rear	6.2	3.1	2	6.5	2.7	2.2	6.3	2.3	1.4
D8	D	Front	5.5	6.9	5.3	6.6	5.4	3.1	6.5	4.8	4.9
		Rear	5.2	4.1	3.9	5.3	4.6	3.4	4	6.8	3.2

[a] D = dispersion fuel.
[b] M = monolithic fuel.

3. Model development

The rate equation for oxide growth on aluminum alloy can be expressed by a power law such as

$$\frac{dx}{dt} = kx^{-p} \tag{1}$$

where x, t, k, and p are the oxide thickness, time, reaction constant and rate-law power, respectively. The integration of Eq. (1) gives the general form of the kinetic equation of aluminum alloy oxidation

$$x = \left[x_0^{p+1} + (p+1)kt\right]^{\frac{1}{p+1}} \tag{2}$$

where x_0 is the film thickness at the start of a test.

Aluminum alloys undergo oxidation if oxygen is available even at room temperature, producing a protective oxide (Al_2O_3). The growth rate saturates in a short time. The rate-law for this type of oxidation has a high rate-law power. The protective oxide, however, degrades in water by the formation of various oxide-hydrates at the outer surface in time, leaving only a thin protective Al_2O_3 layer on the aluminum surface. The most frequently found oxide-hydrates in typical tests are boehmite ($Al_2O_3 \cdot H_2O$) and bayerite ($Al_2O_3 \cdot 3H_2O$). Typically, the bayerite layer is found at the outer surface of the boehmite layer. In the present work, the term 'oxide thickness' generally refers the total thickness of the layers of the protective oxide (Al_2O_3) and hydrated oxides ($Al_2O_3 \cdot H_2O$ and $Al_2O_3 \cdot 3H_2O$). These oxide-hydrates are soluble in water, especially in flowing water, meaning that even the hydrated oxide becomes less protective, further enhancing film growth. As tests of pre-

Table 3
RERTR-7A oxide thickness measurements at 18 locations shown in Fig. 1

Plate ID	Fuel type	Oxide thickness (μm)									
		Front / Rear	A / A	B / B	C / C	D / D	E / E	F / F	G / G	H / H	I / I
A5	D[a]	Front	3.5	2.2	1.1	3.5	1.8	2.4	1.5	0.3	2.3
		Rear	1.6	1.6	0.6	2.4	1.6	1.3	1.2	1.5	2.3
A6	D	Front	1	3.3	1.5	1	0.4	0.2	1.3	0.3	0.4
		Rear	4.6	0.5	0.7	0.9	1	0.5	3.3	0.5	0.6
A7	D	Front	0.4	1	1.4	1.6	0.7	0.5	0.5	1.1	0.4
		Rear	2.9	1.3	2	3.9	0.7	1.1	0.5	1.6	2.4
A8	M[b]	Front	2.7	1.5	3.6	6	0.8	0.4	5.6	1.2	1.2
		Rear	0.4	0.5	9.3	1.9	1.3	1.2	2.4	2.1	0.6
B1	D	Front	3.8	2.4	2.1	2.5	1.7	3.4	2.6	2.5	2.1
		Rear	4.5	3.2	3.4	4.1	2.8	2.7	6.1	2.3	2.2
B2	D	Front	5.2	3	3.2	2.2	2.8	2.2	2.5	3.2	2.5
		Rear	0.4	2.5	2.8	2.6	4.3	2.5	1.2	3.4	1.7
B3	D	Front	4.1	3.7	3.9	2.7	2.9	3.7	5.4	3.6	2.2
		Rear	6.6	5.7	4.1	3.8	3.4	3.4	6.2	2.6	2.7
B4	M	Front	4	3.8	3.2	9.6	4.7	1.4	3.9	1.4	6.6
		Rear	6.1	6.6	4.3	6.1	2.7	3.5	7.2	5.4	6
B5	M	Front	10.4	0.7	6.5	10.3	1	5	11.2	3.1	5.6
		Rear	4.5	0.6	5.8	5.9	2.5	5.7	7	2.8	6
B6	D	Front	8.2	3.2	2.2	7.4	3	2.3	12.6	4.7	4.9
		Rear	7.4	3.9	4	4.7	3.1	4.1	6.4	3.5	2.7
B7	M	Front	4.5	6.7	5.4	10	6	5.2	5.2	4.4	5.7
		Rear	3.7	3.6	3.5	6	5.3	4.7	6.7	4.5	7
B8	M	Front	3.6	3.3	3.7	3.6	2.3	3.6	4	3.2	2.6
		Rear	2.6	1.3	1.5	1.7	2.5	2.1	1.4	2.1	2.7
C1	M	Front	2.6	3.7	5.4	2.4	4.2	6.5	3.8	3.8	6.4
		Rear	9.5	2.2	1.8	6.6	2.2	3.9	7.1	4.2	1.3
C2	M	Front	4.2	11.2	4	0.8	3.4	2.6	3.3	2.7	2.3
		Rear	0.8	3.5	2.9	1.3	4.2	4.2	0.7	4.6	4.9
C3	M	Front	3.4	1.7	3.8	1.9	0.3	2.2	4.2	0.5	2.9
		Rear	5.8	2.1	0.4	5.8	3.3	1.7	7.3	3.3	1.9
C5	M	Front	5.4	2.2	5.2	6.6	2.3	5.5	10.5	4.5	6.8
		Rear	8.7	3	0.8	13.8	2.1	0.9	9.3	8.3	5.9
C6	M	Front	3.5	4.4	3.2	7.2	1	3.2	15.2	0.4	3.7
		Rear	4.2	0.3	5.4	15.7	3.7	0.5	10.1	0.4	1
C7	D	Front	1.5	1.3	6.6	2.5	1.5	2.2	0.6	4.3	1.2
		Rear	7.3	0.3	0.4	8.6	1.6	0.6	15.6	2.1	1.9
C8	D	Front	7.1	1.7	1.6	12.5	0.6	2.4	8	0.4	1.9
		Rear	9.7	0.4	0.8	10.4	0.5	1.4	8.4	0.8	0.8
D1	D	Front	15.3	5.2	2.7	19.2	4.2	3.3	12.1	3.7	1.9
		Rear	7.3	3.3	3.2	4.7	2.8	1	6.5	2.5	3.3
D3	D	Front	10.5	2.3	1.1	6.6	2.5	0.7	2.2	2.3	2.2
		Rear	13.1	4.3	3	11.8	3.6	2.6	14.6	4.2	2.6
D6	M	Front	20.8	4.6	3	20	9.8	4.5	6.8	6.1	4.9
		Rear	17	7.2	10.3	18.2	8.2	8.4	10	7	8
D7	M	Front	8.3	4.1	4.9	8.7	4	3.7	4.9	4.2	4.9
		Rear	12	13.8	9.5	10.6	5.3	2.9	21.3	13.1	1.5
D8	D	Front	1	2.5	1.1	1.5	1.6	2.1	4.4	4	4.3
		Rear	2.1	2.5	1.8	3.1	2	2.5	3	4.7	4.3

[a] D = dispersion fuel.
[b] M = monolithic fuel.

filmed samples showed [15], because boehmite has a higher solubility than bayerite, dissolution is selective in the oxide. Dissolution may take place not exclusively at the oxide–water interface, but within the oxide if cracks and fissures are available. This heterogeneous dissolution or leaching action increases the porosity of the oxide film. In addition, the coexistence of oxide-hydrates provides the cause for crack development in the oxide film. Dillon found that oxide films tested at higher flow rates tend to have higher porosity than those tested at lower flow rates [16].

For oxidation with degraded films, the growth law has a lower p value than the protective oxidation case, depending on the extent of oxide degradation. The degradation of Al_2O_3 and oxide-hydrates is dependent on temperature, water pH, water flow rate, and perhaps irradiation.

Dillon [16] showed that the oxide growth increase with increased oxide solubility. Dickinson and Lobsinger [17] reported the solubilities of oxide and oxide-hydrates as a function of temperature and water pH. The higher the temperature and pH, the higher is the solubility. They also showed that the oxide dissolution rate increases as the water flow rate increases due to the increased porosity in the oxide films as well as to a lower dissolved oxide concentration in the faster-flowing water.

For the present work, the solubility of oxide was formulated based on the equation and data reported in Refs. [15,17], as follows:

$$\ln C_s = -\left(-13.79 - \frac{1211.16}{T_{x/w}}\right)(0.041H^2 - 0.41H - 0.07) \quad (3)$$

where C_s is the oxide solubility in g/g H_2O, $T_{x/w}$ the oxide–water interface temperature in K and H the pH. This solubility is for a generic aluminum hydroxide, viz., a typical combination of boehmite and bayerite. The applicable temperature range is 25–300 °C and the pH must be less or equal to 7.0. Note that Eq. (3) assumes an infinite dilution of the dissolved oxide in the water at the oxide surface. The flow rates in typical reactors are high enough so that this requirement is effectively satisfied. The oxide measurement data reported by Griess [2] and Pawel [5,7] were used to fit simultaneously the rate-law power p as a function of C_s calculated by Eq. (3) and an

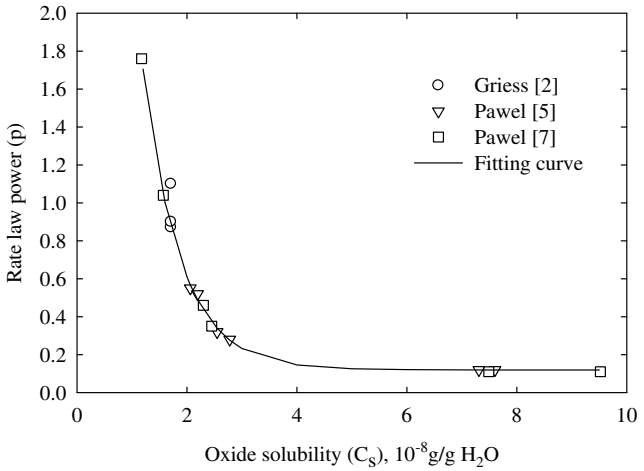

Fig. 3. Curve fitting of rate-law power (p) as a function of oxide solubility (C_s). Data found in the literature were used to calculate p and C_s that are suitable to give the oxide thicknesses.

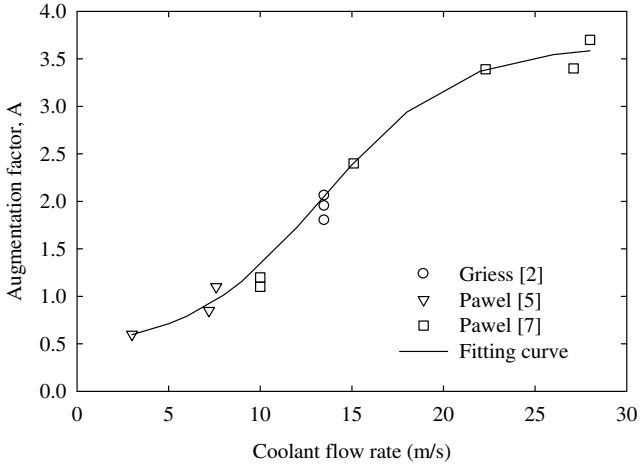

Fig. 4. Curve fitting of augmentation factor (A) as a function of test flow rate (v_c). Data found in the literature were used to calculate A versus v_c that are suitable to give the oxide thicknesses.

augmentation factor A that accounts for the effect of flow velocity. The data fitting resulted in the p correlation as follows:

$$p = 0.12 + 9.22 \exp\left(-\frac{C_s}{6.82 \times 10^{-9}}\right) \quad (4)$$

No data for oxide dissolution as a function of flow velocity were found. However, an increase in coolant velocity seems to enhance oxide growth by degrading the oxide film integrity. The effect of coolant velocity on oxide growth is taken into account by the augmentation factor, which is correlated with the coolant velocity using the following sigmoidal function:

$$A = 0.43 + \frac{3.21}{1 + \exp\left(-\frac{v_c - 13.39}{3.60}\right)} \quad (5)$$

where v_c is the coolant flow rate in m/s. The range of coolant velocity fitted is 3–28 m/s. In Figs. 3 and 4 the curve fitting results are compared with the data.

The oxide film develops cracks under a high heat flux due to stress buildup, which is another mechanism for porosity increase in the oxide film together with heterogeneous oxide dissolution. The stress buildup is proportional to the temperature drop across the oxide film. The cracking is the direct cause of oxide spallation encountered frequently in thick oxide films. Neither Pawel nor Kritz tried to predict the time of spallation; however, they noticed that the higher heat flux reduces the apparent activation energy, yielding a higher growth rate. Although the effect of the heat flux is manifested by a combination of other variables such as the oxide thickness and its thermal conductivity, they added a term to the surface temperature proportional to the heat flux, and neglected the effect of the changing oxide thickness. They also assumed a constant thermal conductivity of the oxide film, viz., 2.25 W/m-K [2,5]. For these reasons, their models cannot predict the accelerated film growth as the oxide thickness increases, particularly near spallation. In the present model, the effect of the porosity buildup due to cracking and heterogeneous oxide dissolution in the oxide film growth was modeled considering the following. The oxide thermal conductivity decreases as the oxide thickens, and the reaction temperature varies as a function of oxide thickness, thermal conductivity, heat flux, and the extent of oxide degradation.

Postirradiation micrographs [1,5,8,11–13] revealed that thin oxide films were free of cracks or pores, which suggested that the thermal conductivity degradation of thin oxides is negligible. As the oxide film thickened further, however, its thermal conductivity decreased due to porosity increase (or crack development). After reviewing the data [1–5,8–13,18], the threshold thickness was tentatively set at 25 μm. The decrease was assessed by an empirical function of the oxide thickness at a rate giving k_T = 1.85 W/m-K at x = 50 μm, which was deduced from the data reported by Griess [1]. The temperature dependence of the oxide thermal conductivity was not available in the literature. Therefore, it was considered constant with respect to temperature. Consequently, the oxide thermal conductivity was formulated as a function of the oxide thickness as follows:

$$\begin{aligned} k_T &= 2.25, && \text{for } x \leqslant 25, \\ k_T &= 2.25 - 0.016(x - 25), && \text{for } 25 \leqslant x \leqslant 100 \end{aligned} \quad (6)$$

where k_T is in W/m-K and x in μm.

The temperature difference across the oxide film can be calculated by

$$\Delta T = \frac{qx}{k_T} \quad (7)$$

where q is the heat flux, x the oxide film thickness, and k_T the effective thermal conductivity of the oxide film.

The reaction temperature governing the Al oxidation reaction in steam is known to be the metal–oxide interface temperature [1,17]. In this situation, the oxidant transport through the oxide is the reaction controlling process. For thin oxides, since ΔT across the oxide film is small, the use of oxide–water interface temperature ($T_{x/w}$) as the reaction temperature is considered acceptable. However, this will cause a considerable under prediction in the oxide thickness calculation for a situation with a high ΔT, which prevails for a thick oxide with high porosity and a high heat flux.

A modification to the reaction temperature can be formulated by adding the temperature difference across the oxide film with a fitting adjustment to consider the porous nature of the oxide. The effect is correlated in the reaction constant k as follows:

$$k = 3.9 \times 10^5 \exp\left(\frac{-6071}{T_{x/w} + AB\frac{qx}{k_T}}\right) \quad (8)$$

where $T_{x/w}$ is the oxide–water interface temperature in K, q is the surface heat flux in MW/m^2, x in μm, and k_T in W/m-K. The pre-exponential factor and activation energy were fitted to the out-of-pile data available in the literature. The augmentation factor, A, is added as a multiplier to take into consideration the effect of coolant velocity. The augmentation factor increases as the coolant velocity increases, as can be seen in Eq. (5). Because of the water access through the defected oxide, the effective distance that the oxidant migrates through the oxide to the metal–oxide interface decreases. A correction factor, B, is needed to account for the reduction in the 'oxide thickness' for oxidant migration. The best fit using the in-pile data [8–12] resulted in B = 0.37. The fitting results with B = 0.37 are compared between the in-pile data and the model predictions in Figs. 5–10.

It should be noted that because x and k are coupled, the equations were solved iteratively. The time interval in fitting Eq. (8) was set to 24 h, and the value of x at the previous time step was used to avoid endless iteration.

In Figs. 5 and 6 the measured data from the UMUS tests in HFR-Petten [8,12] are compared with the predictions. The measured film thickness data were obtained from the optical metallographic pictures of Ref. [8]. Temperatures were calculated based on the power histories of HFR-Petten. The axial heat flux distribution was obtained based on the gamma scan result, and the plate powers were available from ANL-CEA joint work [9]. The coolant enters from the top of the core in the UMUS and SIMONE tests [8,12].

Fig. 5 shows the prediction result for the sample section (12 × 19 mm) cut at 90 mm from the bottom of a lower power plate (U7MQ2005) irradiated from the UMUS test, where the

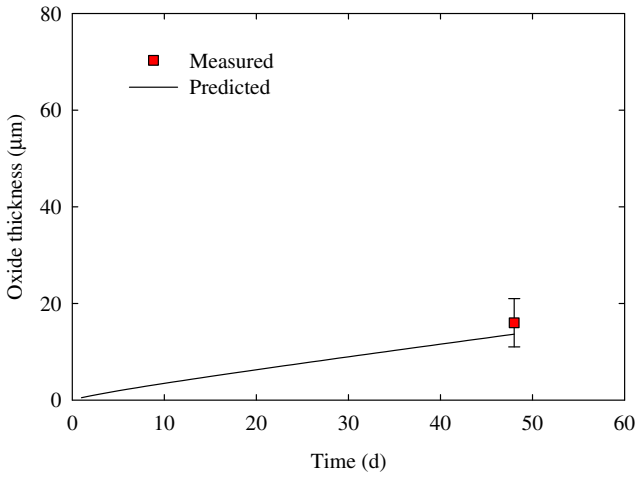

Fig. 5. UMUS U7MQ2005 (LEU) sample at 90 mm from plate bottom. The test parameters are $T_{x/w}$ = 82.6 °C, q = 1.7 MW/m^2, pH 6.5, and v_c = 8.3 m/s. The prediction is made with B = 0.37 in Eq. (8).

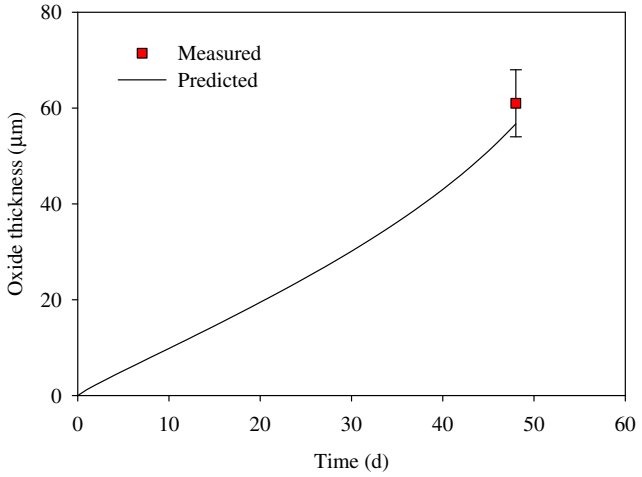

Fig. 6. UMUS U7MR3505 (MEU) sample at 274 mm from plate bottom. The test parameters are $T_{x/w}$ = 107.4 °C, q = 2.5 MW/m^2, pH 6.5, and v_c = 8.3 m/s. The prediction is made with B = 0.37 in Eq. (8).

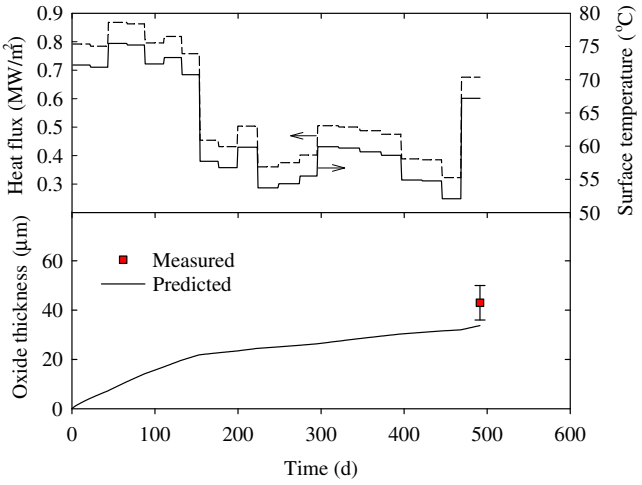

Fig. 7. SIMONE LC-04 plate tested at HFR comparison at the center of plate. The additional test parameters except temperature and heat flux are pH 6.5 and v_c = 6.6 m/s. The prediction is made with B = 0.37 in Eq. (8).

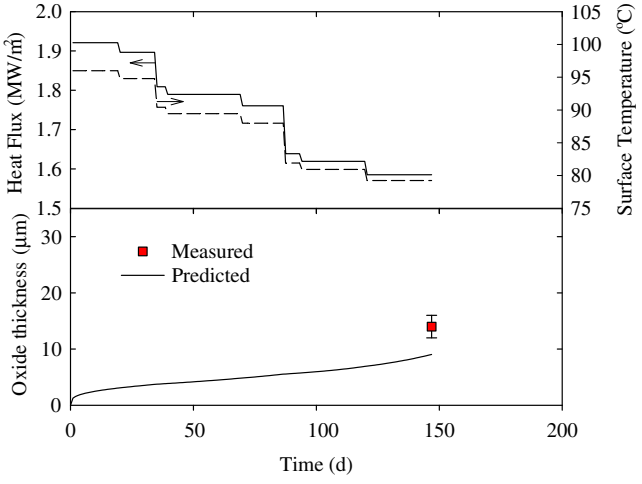

Fig. 8. Miniplate A101 irradiated in ORR. The additional test parameters except temperature and heat flux are pH 5.5–6.3 and v_c = 8.5 m/s. The prediction is made with B = 0.37 in Eq. (8).

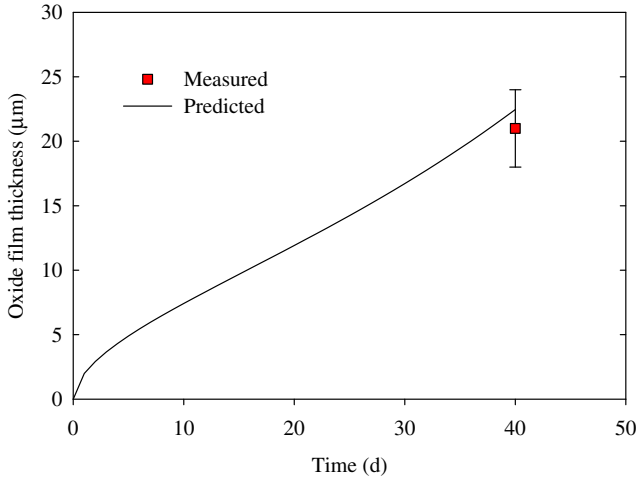

Fig. 9. Comparison for U7MTBR06 (right plate) from FUTURE test in BR-2. The measured oxide thickness is for the peak oxide at 12 mm right of the centerline. The test parameters are v_c = 12 m/s, $T_{x/w}$ = 122 → 109 °C linearly with time, q = 3.2 → 2.7 MW/m^2 linearly with time, pH 5.9 → 6.2 linearly with time [9,10]. The prediction is made with B = 0.37 in Eq. (8).

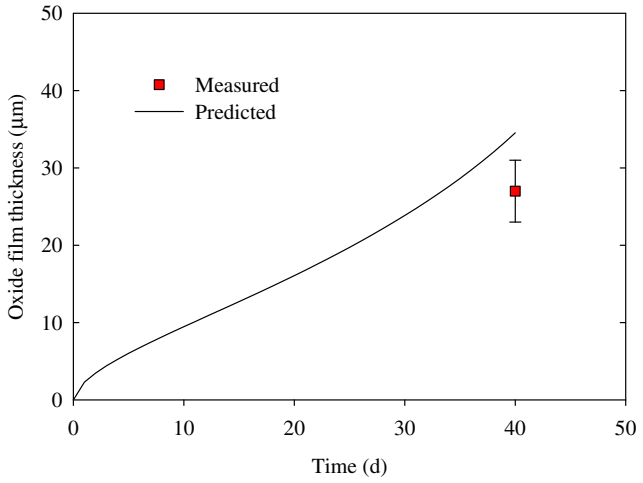

Fig. 10. Comparison for U7MTBR06 (left plate) from FUTURE test in BR-2. The measured oxide thickness is for the peak oxide at 12 mm left of the centerline. The test parameters are v_c = 12 m/s, $T_{x/w}$ = 128 → 116 °C, q = 3.4 → 2.9 MW/m^2, pH 5.9 → 6.2 [9,10]. The prediction is made with B = 0.37 in Eq. (8).

oxide–water interface temperature was 82.6 °C, heat flux 1.7 MW/m^2, coolant flow velocity 8.3 m/s and pH 6.5. The error bar indicates the range of the minimum and maximum of the measured data at six locations, three on each surface, in the sample section. Another prediction was made for a higher power plate (U7MR3505) from the UMUS test, as shown in Fig. 6. The sample section (12 × 19 mm) was cut from the plate 274 mm from the plate bottom, where the power had been the highest in the plate. Oxide spallation was observed at the center region of the sample section [9]. The measurement at the oxide spallation was excluded from obtaining the error bar. The oxide spallation behavior was well simulated by the model; the accelerated film growth in a short time at the final stage of the test indicates the possibility of spallation.

For the SIMONE LC-04 test [11,12], a prediction was made and shown in Fig. 7. The measured data were obtained from the optical metallographic pictures contained in Refs. [11,12]. The oxide–water interface temperature and heat flux were calculated based

on the power histories, coolant flow condition, and inlet temperatures available in the literature.

A calculation for the miniplate test from ORR was made, and the result is shown in Fig. 8. The test was conducted by ANL with collaboration with ORNL in mid-1980s. The miniplate A101 is approximately one-fifth of the standard plate in length, in contrast to the curved shape of the standard plates. Five modules including the reduced-length plates were stacked in a module holder. The oxide thickness was measured at the center of the plate. The heat flux and surface temperature of the A101 plate at the center location for the module were calculated based on the power history. The coolant pH was varied in the range of 5.5–6.3. The prediction was made assuming that the pH changed from 5.5 to 6.3 linearly with time.

Predictions for two FUTURE test plates were also made and compared. In Fig. 9, a prediction for U7MTBR06 (right plate) from the FUTURE test in the BR-2 reactor [9,10] was made using the coolant velocity of 12 m/s and varying the plate surface temperature, heat flux and pH, from 122 to 109 °C, from 3.2 to 2.7 MW/m^2 and from 5.9 to 6.2 linearly with time, respectively. The heat flux and temperature are at the location where the oxide thickness was measured. The oxide thickness was measured on the parallel line 12 mm apart to the right of the plate axial centerline. In Fig. 10, a prediction for U7MTBR06 (left plate) from the FUTURE test in the BR-2 reactor [9,10] was made using the coolant velocity of 12 m/s and varying the plate surface temperature, heat flux and pH, from 128 to 116 °C, from 3.4 to 2.9 MW/m^2 and from 5.9 to 6.2 linearly with time, respectively. The measured oxide thickness was obtained on the parallel line 12 mm apart to the left of the plate axial centerline.

In general, the model calculations are close to the measured data, which confirms the validity of the correction factor $B = 0.37$ in Eq. (8) and the model as well. However, for some cases, there were inconsistencies of the model predictions to the measured values. These are assumed to result from inaccurate input data, i.e., oxide–water interface temperature, heat flux, pH and coolant flow rate as a function of time. If an accurate power history is given, the oxide–water interface temperature and heat flux are calculated accurately. However, coolant flow rate and pH are generally stated as a range, so average values were used. This leads to inaccurate results, because the model is sensitive to these input data in the pH range of 5–7.

Table 4
Comparison of oxide thickness between measured and predicted for RERTR-6 and 7A test plates (μm)

	Fuel type	Measured	Predicted
RERTR-6			
B2 (R2R020)	Dispersion	4 ± 0.4	4.1
B5 (R3R030)	Dispersion	5 ± 0.5	6
B7 (L1F040)	Monolithic	4 ± 1.0	4.7
RERTR-7A			
B2 (R2R040)	Dispersion	4 ± 0.4	4.1
B7 (L1F140)	Monolithic	6 ± 1.5	4.7

4. Model predictions for RERTR test plates

Several predictions were made for plates from the RERTR-6 and 7A tests and the results are given in Table 4. The measured data for the corresponding plates used for predictions are also given in Table 4 for comparison with the predictions. The average values are given between the front and rear surface measurements at location E shown in Fig. 2. Considering the measurement errors, the predictions are fairly consistent with the measured values. Discrepancies are found for B5 dispersion fuel plate from the RERTR-6 test and B7 monolithic fuel plate from the RERTR-7A.

The input data needed for model predictions are the test duration, coolant pH, coolant flow velocity, cladding surface heat flux, and oxide–water interface temperature. The coolant pH and flow rate are considered to be relatively accurate because they were obtained from the reactor operation parameters. Since they were calculated by a computer code PLATE [19] based on the assumption that the fuels were uniformly loaded in the plate, the cladding surface heat flux and temperature data cause most uncertainties. Post-irradiation examination showed that fuel loading in some dispersion fuel plates, particularly from the RERTR-7A test, is irregular in relative to the monolithic fuel plates. Because of fabrication difficulty, however, monolithic fuel plates have less uniform cladding thickness than the dispersion fuel plates.

5. Discussion

5.1. RERTR test data

The oxide thickness data from the RERTR-6 and 7A tests are substantially lower than other in-pile test data measured at foreign reactors (see Table 5). The growth is even less than out-of-pile test results from Refs. [1–5,7]. The low oxide buildup is partly attributed to the effect of prefilming, but it is probably more due to the effect of low pH in the ATR. The pH in the ATR was controlled in the range 5.1–5.3 and other reactors analyzed in this study were at 5.9–6.5. However, in the pH range of 5.0–6.0, the oxide growth rate is very sensitive to pH [7]. A slight error in pH reading can result in a significant change in the calculated oxide thickness. This is probably one of the main reasons that the test results in this range typically show the most uncertainty. The effect of pH on oxide thickness growth in the present model is shown in Fig. 11.

Table 5
Oxide thickness data and predictions by models (μm)

	Measured	Griess (RF = 2.7)[a]	Kritz	Pawel (RF = 16)[b]	Present study	Ref. for measured data
UMUS LEU 90 mm	16 ± 5	14.1	13.5	6.3	13.6	[8]
UMUS MEU 274 mm	61 ± 7	32.9	28.1	22.3	56.7	[8]
SIMONE LC-04	43 ± 7	41.9	21.4	12.1	33.7	[11,12]
ORR A101	14 ± 2	40.5	35.7	19.5	9.0	Present study
FUTURE right plate	21 ± 3	36.7	32.4	29.1	22.5	[10]
FUTURE left plate	27 ± 4	44.8	37.0	39.1	34.5	[10]
RERTR-6 B2	4 ± 0.4	45.9	18.1	22.4	4.1	Present study
RERTR-6 B5	5 ± 0.5	81.2	24.6	52.5	6.0	Present study
RERTR-6 B7	4 ± 1.0	58.4	17.2	31.8	4.7	Present study
RERTR-7A B2	4 ± 0.4	38.2	32.7	21.3	4.1	Present study
RERTR-7A B7	6 ± 1.5	47.3	38.3	29.3	4.7	Present study

[a] A rate factor (RF) of 2.7 was multiplied to the rate constant in Eq. (10) as suggested by Griess [2] for the pH range of 5.7–7.0.
[b] A rate factor (RF) of 16 obtained from Fig. 3.9 of Ref. [7] was multiplied to the rate constant in Eq. (13) to compensate the pH effect.

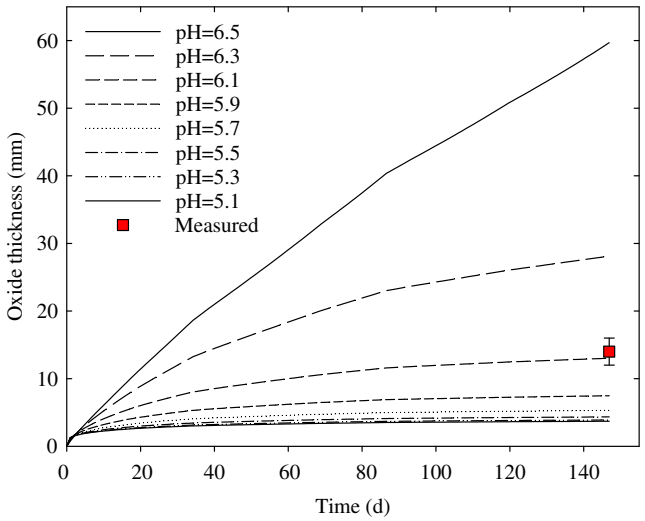

Fig. 11. Effect of pH on oxide growth predicted by the present model for miniplate A101 irradiated in ORR. The same input test parameters were used as in Fig. 8 except pH.

5.2. Model validation

The Griess model was developed in 1960s [1,2]. It used the kinetic equation given in Eq. (2) with $p = 0.28535$

$$x = \left(x_0^{1.28535} + 1.28535kt\right)^{0.778} \tag{9}$$

where x, x_0, t are film thickness (μm) at time t, film thickness (μm) at time zero, and time (h), respectively. The rate constant k is

$$k = 1.2538 \times 10^5 \exp\left(\frac{-5913}{T_{x/w}}\right) \tag{10}$$

As seen in Eq. (10), the rate constant is only dependent on oxide–water interface temperature. The other variables, which affect the growth rate, were assumed fixed. The Griess model is applicable for pH of 5, water flow rate of ~12 m/s and short duration of 10–20 days. The model was recommended to be applicable for the pH range of 5.7–7.0 by using a pre-exponential factor of 3.3853×10^5, viz., a factor of 2.7 multiplied to k in Eq. (10).

The Kritz model [3] has the same kinetic equation as the Griess model, i.e., Eq. (9). The rate constant, however, is different, i.e.

$$k = 8.686q^{1.28535} \exp\left(\frac{-2416.5}{T_{x/w}}\right) \tag{11}$$

where q is heat flux at the oxide–water interface in MW/m^2. The Kritz model is intended to be applicable for pH 5.0.

An updated version of ANS Correlation II was reported by Pawel et al. [4–6]. They adopted the same kinetic equation given in Eq. (2) with $p = 0.351$

$$x = \left(x_0^{1.351} + 1.351kt\right)^{0.74} \tag{12}$$

The corresponding rate constant was

$$k = 6.388 \times 10^7 \exp\left(\frac{-9154}{T_{x/w} + 1.056q}\right) \tag{13}$$

where q is heat flux at the oxide–water interface in MW/m^2. In this model, the reaction temperature is allowed to increase by adding a heat flux term to the oxide–water interface temperature. Pawel et al. also studied the effect of pH on oxide film growth [7]. A rate factor as a function of pH can be obtained from Ref. [7] that is to be multiplied to the rate constant in Eq. (13).

The reaction temperature of Griess and Kritz models is the temperature at the oxide–water interface although they use the rate constants fitted to the oxide thickness data. As seen in Eq. (13), the reaction temperature of the Pawel model was obtained by adding a term linearly proportional to the heat flux to the oxide–water interface temperature. The reaction temperature of the Pawel model is independent of the oxide thickness and property. Since it relies on a constant proportionality on heat flux, this model tends to produce over predictions for thin oxides and under predictions for oxides thicker than ~20 μm.

In Table 5, the measured data from various in-pile tests and predictions by the models are compared. The Griess model with a rate factor of 2.7 multiplied to the reaction constant predicts generally higher than the measured postirradiation data, particularly the results for the RERTR-6 and 7A test plates are excessively overpredicted. The Kritz model without any correction for the pH other than 5.0 also poorly predicted the measured data. The Pawel model augmented by a rate factor of 16 for the pH range of 5.8–6.5 predicted also inconsistently for most cases. These models exhibited a similar trend; lower predictions than the measured for UMUS and SIMONE and higher predictions than the measured for all others. The inability of accounting for the effect of pH is the probable reason for this discrepancy. In contrast to the existing models in the literature, the present model predicted all test data very well.

The deficiency in the models in the literature primarily lies in their inability to cope with various situations where a different rate-law is required according to the extent of oxide degradation. They all use constant rate-law powers regardless of the property of the oxide film. As shown in Fig. 12, for example, the model developed in the present work has a variable rate-law power. The rate-law power, p, in the present model is considered as an effective variable changing with the temperature and pH. As temperature increases p decreases and in turn increases oxide growth. An increase in temperature promotes oxide growth in two ways. One is a direct increase in the oxidation reaction, and the other is an indirect increase by degrading the protective oxide. The degradation of the protective oxide effectively reduces the distance for oxygen transport, hence increase in oxide growth.

An increase in pH increases oxide dissolution and enhances the degradation of the oxide. This also increases oxide growth by decreasing p. Although the boehmite has a higher dissolution rate than the bayerite and, hence, selective leaching occurs more for the boehmite, it is expected that the overall oxide thickness decreases. However, in-pile test data used in this study [11,16] and fitting results showed that a high pH favors oxide growth rather than

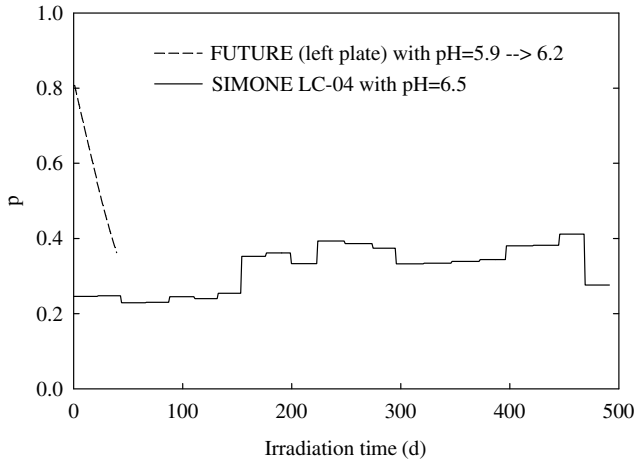

Fig. 12. Rate-law powers (p) versus time for SIMONE LC-04 plate and for U7MTBR06 (left plate) from FUTURE test in BR-2.

thinning. The pH effect on oxide growth appears to be larger for oxides thicker than a threshold value. Using the density of boehmite ($Al_2O_3 \cdot H_2O$) of 3.02 g/cm^3, Griess reported that about half of the oxide thickness is dissolved at pH 5 [2]. This did not even include the presence of bayerite ($Al_2O_3 \cdot 3H_2O$) that has a lower density and less solubility than boehmite. This suggests that the measured oxide thickness data are the result of combination of continuous buildup and dissolution of the oxides. In the present model, no attempt was made to explore the kinetics of cladding wall thinning and oxide dissolution. Furthermore, separation of the kinetics of oxide buildup and dissolution was not tried. The present model is developed based on oxide thickness data after irradiation tests. In this regard, the model predicts an 'effective' oxide thickness.

For thin oxides measured in the RERTR tests, the measurement uncertainty and prediction error increase. As is evidenced in Tables 2 and 3, some oxide thickness measurements are less than the average prefilm thickness (~1 μm). This may be due to measurement errors or instability caused by oxide dissolution. This suggests that model predictions for thin oxide layers are less reliable.

Acidic coolant dissolves the internal surfaces of the reactor coolant system. The ions, dominantly Fe-ions, contained in the coolant deposit on the cladding and typically found in the outer oxide layer. The typical deposit layer from loop tests was 1–2 μm and its buildup reduces the underlying corrosion product growth [5]. However, the deposition rate was known to be minimal for most reactor situations where the coolant pH was higher than 5 and inlet temperature was high enough [4]. In the present model, this effect was taken into account in the reaction rate constant k implicitly.

The Griess data [1,2] were obtained for alloy Al 6061 and Al 1100, the Kritz data [3] were for Al 8001, and the Pawel data [4–6] were for pure Al, Al 1100, Al 6061 and Al 8001. The authors found no significant difference in the oxidation rate of these alloys, although different behavior associated with spalling and internal reactions was observed. The cladding type for UMUS, SIMONE and FUTURE tests is AG3NE (3%Mg + Al balance) and that for A101 and RERTR tests is Al 6061 (1%Mg + Al balance; see Section 2 for details). We saw no discernable effect with respect to alloy types on the oxide thickness. Therefore, it is our view that the present model is also applicable to these alloys.

Other parameters that have an indirect effect on the oxidation rate were coolant electrical conductivity and coolant inlet temperature. These parameters were not incorporated into the model because they were considered to be redundant to the variables already in the correlations.

6. Conclusions

The waterside oxide thicknesses measured on the aluminum alloy cladding from the RERTR tests were substantially lower than those measured from other reactors available in the literature. Prefilming may be one of the reasons. However, the main reason is believed to be due to the lower pH (pH 5.1–5.3) of the primary water in the ATR than in the other reactors (pH 5.9–6.5).

An empirical model to predict the oxide film thickness on aluminum alloy cladding has been developed as a function of irradiation time, temperature, surface heat flux, pH, and coolant flow rate. The applicable ranges of pH and coolant flow rates cover most research and test reactors. The predictions by the new model were in good agreement with the in-pile test data available in the literature as well as with the RERTR test data from the ATR. For better predictions by the model, precise records of temperature, surface heat flux, pH, and coolant flow rate as a function of irradiation time are necessary.

Acknowledgments

The authors thank Mr. F. Huet from CEA and Mr. F. Wijtsma from NRG Petten for their permission for the authors to use their data. One of the authors (YSK) is grateful to Dr. Ho Jin Ryu from KAERI for his helpful comments.

References

[1] J.C. Griess, H.C. Savage, J.G. Rainwater, T.H. Mauney, J.L. English, ORNL-3230, Oak Ridge National Laboratory, 1961.
[2] J.C. Griess, H.C. Savage, J.L. English, ORNL-3541, Oak Ridge National Laboratory, 1964.
[3] R.S. Ondrejcin, DPST-83-324, Savannah River Laboratory, 1983.
[4] R.E. Pawel, G.L. Yoder, D.K. Felde, B.H. Montgomery, M.T. Mcfee, Oxidat. Met. 36 (1/2) (1991) 175.
[5] R.E. Pawel, D.K. Felde, J.A. Clinard, T.A. Thornton, in: Corrosion 93, The NACE Annual Conference and Corrosion Show, 188/1, 1993.
[6] Y.S. Kim, G.L. Hofman, N. Hanan, J.L. Snelgrove, in: Proceedings of the International Meeting on Reduced Enrichment for Research and Test Reactors, Chicago, IL, USA, October 5–10, 2003, Available from: <http://www.rertr.anl.gov/index.html>.
[7] S.J. Pawel, D.K. Felde, R.E. Pawel, ORNL/TM-13083, Oak Ridge National Laboratory, 1995.
[8] A. Languille, D. Planco, F. Huet, B. Guigon, P. Lemoine, P. Sarristan, G.L. Hofman, J.L. Snelgrove, J. Rest, S.L. Hayes, M.K. Meyer, H. Vacelet, E. Leborgne, D. Dassel, in: ENS RRFM 2002 Trans. 6th International Topical Meeting on Research Reactor Fuel Management, Ghent, Belgium, March 17–20, 2002.
[9] F. Huet, B. Guigon, P. Lemoine, C. Jarousse, F. Wijtsma, G. Dassel, G.L. Hofman, J.L. Snelgrove, in: ENS RRFM 2003 Trans. 7th International Topical Meeting on Research Reactor Fuel Management, Aix-en-Provence, France, March 9–12, 2003.
[10] F. Huet, Private communication, CEA-Cadarache, France, 2003.
[11] G.L. Hofman, Y. Fanjas, H. Pruimboom, and F. Wijtsma, in: Proceedings of the International Meeting on Reduced Enrichment for Research and Test Reactors, October 4–7, 1993, Oarai, Japan, JAERI Report, JAERI-M-94-042, March 1994, Available from: <http://www.rertr.anl.gov/index.html>.
[12] F. Wijtsma, Private communication, NRG Petten, The Netherlands, 2008.
[13] A. Leenaers, E. Koonen, Y. Parthoens, P. Lemoine, S. Van den Berghe, J. Nucl. Mater. 375 (2008) 243.
[14] F. Garzarolli, E. Steinberg, H.G. Weidinger, in: Zirconium in the Nuclear Industry: 8th International Symposium, ASTM STP 1023, L.E.P Van Swam and C.M. Eucken, eds., American Society of Testing and Materials, Philadelphia, 1978, and references therein, p. 202.
[15] M.J. Graber, G.W. Gibson, V.A. Walker, W.C. Francis, IDO-16958, US AEC, 1964.
[16] R.L. Dillon, HW-61089, Hanford Laboratory, 1959.
[17] D.R. Dickinson, R.J. Lobsinger, HW-77529, Hanford Laboratory, 1963.
[18] R.L. Sindelar, P.S. Lam, M.R. Louthan Jr., N.C. Iyer, Mater. Character. 43 (1999) 147.
[19] S.L. Hayes, G.L. Hofman, M.K. Meyer, J. Rest, J.L. Snelgrove, in: Proceedings of the International Meeting on Reduced Enrichment for Research and Test Reactors, San Carlos de Bariloche, Argentina, November 3–8, 2002, Available from: <http://www.rertr.anl.gov/index.html>.